Technical Note

Field Verification of Vehicle-Mounted All-Fiber Coherent Wind Measurement Lidar Based on Four-Beam Vertical Azimuth Display Scanning

Xiaojie Zhang [1], Qingsong Li [1], Yujie Wang [1,2], Jing Fang [1] and Yuefeng Zhao [1,*]

[1] Provincial Engineering and Technical Center of Light Manipulations & Shandong Provincial Key Laboratory of Optics and Photonic Device, School of Physics and Electronics, Shandong Normal University, Jinan 250014, China; 2020020590@stu.sdnu.edu.cn (X.Z.); 2021317041@stu.sdnu.edu.cn (Q.L.); 2021020631@stu.sdnu.edu.cn (Y.W.); fangjing@sdnu.edu.cn (J.F.)

[2] State Key Laboratory of Information Engineering in Surveying, Mapping and Remote Sensing, Wuhan University, Wuhan 430072, China

[*] Correspondence: yuefengzhao@sdnu.edu.cn

Abstract: Wind parameters play a vital role in studying atmospheric dynamics and climate change. In this study, a vehicle-mounted coherent wind measurement Lidar (CWML) with a wavelength of 1.55 μm is demonstrated based on a four-beam vertical azimuth display (VAD) scanning mode, and a method to estimate wind vector from power spectrum is proposed. The feasibility of the application of wind profile Lidar in vehicles is verified by calibration tests, comparison experiments, and continuous observation experiments, successively. The effective detection height of Lidar can reach 3 km. In contrasting experiments, the correlation coefficients of the magnitude and direction of horizontal wind speed measured by vehicle-mounted Lidar and fixed Lidar are 0.94 and 0.91, respectively. The experimental results reveal that the accuracies of wind speed and direction measurements with the vehicle-mounted CWML are better than 0.58 m/s and 4.20°, respectively. Furthermore, to understand the role of the wind field in the process of energy and material transport further, a proton-transfer reaction time-of-flight mass spectrometer (PTR-TOF-MS) is utilized to measure the concentration of volatile organic compounds (VOCs). Relevant experimental results indicate that the local meteorological conditions, including wind speed and humidity, influence the VOC concentrations.

Keywords: motion compensation; spectral signal processing; vehicle mounted; coherent wind measurement Lidar

1. Introduction

Wind fields provide direct power for exchanging energy and matter in the atmosphere [1]. The study of atmospheric wind fields is critical for analyzing global climate change, such as the prediction of disaster weather [2], aviation meteorological safety [3], wind power generation [4,5], etc. Due to their near detection range, low detection accuracy, high cost, and difficulty in recovery, passive methods cannot meet the actual requirements. In contrast, active detection equipment offers apparent advantages in monitoring regional wind fields. With the development of laser technology, the development of Lidar also continues to mature. Over time, the development of coherent Lidar has gone through three stages: gas phase [6], solid phase [7], and all-fiber coherent wind measurement Lidar (CWML) [8,9]. The wavelength of the laser has also changed from 10.6 μm [10] to 1.06 μm, and then to 2.0 μm [11] and 1.5 μm [12]. Recently, a 1.55 μm band all-fiber CWML has been widely used as the remote wind sensor for environmental wind field monitoring, owing to its advantages of high detection accuracy and strong anti-interference [13]. Wind-profile Lidar mainly takes clear-air turbulence (CAT) as the detection object. Wind shear is

essential for Kelvin Helmholtz (KH) waves, which are an important source of CAT. CAT is important for aviation meteorological safety and pollution transfer [14]. The vertical wind shear changes are attributable to the local thermal wind response to the meridional temperature gradient changes. Lee et al. [15] suggest that climate modeling studies on the response of jet streams to climate change should therefore include a consideration of vertical shear as well as speed.

Considering the ever-increasing atmospheric pollution, many scholars from various countries are now committed to the research of atmospheric wind fields. At present, there exist many examples of ground-based CWML [16,17]. However, the literature on vehicle-mounted [18], shipborne [19,20], and airborne [21,22] CWML is scarce. The existing ground-based monitoring stations have largely achieved continuous real-time monitoring of pollutants at fixed points. However, ground-based detection alone makes it difficult to reveal the fundamental issues of pollution formation, sources, and transport impacts. Compared to ground-based Lidar, a mobile Lidar allows for the non-contact monitoring of pollutant emission sources and the tracking of pollutant dispersion, and its measurement range and measurement height are greatly enhanced. Vehicle-mounted CWML is necessary for environmental monitoring. For this necessity, the all-fiber detection system uses optical fiber as the gain medium, which has the advantages of a compact structure, a stable system, and low power consumption [8,9]. The application of fiber-optic elements to vehicle-mounted Lidar considerably enhances fabrication, alignment, and long-term stability. However, the issue of the "vehicle-mounted" CWML is the degradation of wind measurement accuracy caused by vehicle motion. Therefore, a new technique for motion compensation is required.

Motion CWML overestimates the wind vector compared to the fixed Lidars. The question of "how to accurately measure wind field on a moving platform in real time" indicates a problem that still needs to be resolved comprehensively. Following this issue, different methods have been proposed to mitigate the motion-induced error in wind vector estimates from Lidar systems. Achtert, P et al. [23] demonstrated that a combination of commercial Doppler Lidar with a custom-made motion-stabilization platform enables the effective retrieval of wind profiles. Furthermore, Felix Kelberlau et al. [24] proposed a method that uses line-of-sight (LOS) measurements of the Lidar and high-frequency motion data to compensate for the motion error. Zehou Yang et al. [18] suggested a method that utilizes a mobile all-fiber Doppler wind Lidar based on a real-time motion wind retrieval algorithm method. The majority of the existing studies rely on postprocessing, which has certain limitations. However, many application scenarios, such as wind shear alarms, weather disaster prevention and control, and climate analysis, require real-time processing. N. Kotake et al. [25] built a coherent Doppler Lidar with a fiber-based configuration and evaluated its motion compensation function on a motion test platform. Unfortunately, the motion patterns were very limited, especially for the motion frequency. Lidar requires all-weather measurements. Single inertial navigation systems (INS) have the disadvantage of accumulating navigation errors over time. In this paper, the four-parameter method is applied to describe the motion deviation of a vehicle-mounted platform, and a new combined navigation system (CNS) is proposed for motion compensation. Mounting the dual global positioning system (GPS) antennas in the heading direction of the CNS enables the dual GPS to measure the position of two points and calculate the baseline heading to provide the initial heading. Furthermore, when one of the GPS antennas fails to be received, it is supplemented by observations from the INS, which are fed into the algorithm as measurements of the motion error. Therefore, it can overcome the influence of the attitude and speed of the platform motion on the extraction of Doppler frequency shift.

To further validate the application of the vehicle-mounted CWML in environmental management, a preliminary analysis of the relationship between atmospheric wind fields and volatile organic compounds (VOCs) is also presented. VOCs are a complex group of organic substances that are highly volatile at room temperature, including hydrocarbons, oxygen-containing hydrocarbons, halogen-containing hydrocarbons, nitrogen

hydrocarbons, sulfur hydrocarbons, low-boiling-point polycyclic aromatic hydrocarbons, and other complex components. VOCs originate from various biological and technological processes, and their levels in the air are very low, ranging from ppm (10^{-12}) to ppm (10^{-6}). Therefore, effective detection and analysis of the VOCs is essential. Conventional gas chromatography-mass spectrometry (GC-MS) [26] can detect and analyze static or slowly changing VOCs, but is unable to analyze VOCs with constantly changing concentrations in real time. Alternatively, direct injection mass spectrometry (DIMS) [27], with its real-time online analysis capability, offers a new approach for the detection and analysis of VOCs. Over the years, several DIMS techniques have been applied for the detection of VOCs based on the development of ionization techniques and mass detectors. Among them, proton transfer reaction mass spectrometry (PTR-MS) [28,29] is the most mature approach. Compared to conventional mass spectrometry techniques, PTR-MS offers a higher sensitivity and saves time and effort in analyzing VOCs by eliminating the need for sample pre-processing [29]. To further understand the role of wind fields in the process of energy and material transport, concentrations of different groups of VOCs are detected using the proton transfer reaction time-of-flight mass spectrometer (PTR-TOF-MS) at three sampling sites simultaneously.

Accordingly, this study reports the development of a vehicle-mounted CWML with a wavelength of 1.55 μm. In this paper, we propose a method for calculating radial velocities from smoothed accumulated spectra to estimate wind vectors using the velocity azimuth display (VAD) scanning technique. The computational speed of the method can be greatly improved by dividing range gates for each radial direction and applying the same data processing to the signal of each range gate. Furthermore, the method can significantly reduce the impact of bad radial wind estimates and can provide effective results in low carrier-to-noise ratio (CNR) regions. The effectiveness of the proposed CWML is validated via calibration experiments, comparison experiments, and continuous observation experiments. Furthermore, the effect of atmospheric wind fields on the variation in VOCs is reported.

The remainder of this paper is organized as follows: In Section 2, the materials and methods are described. In Section 3, the results and discussion are listed. Finally, the conclusions are presented in Section 4.

2. Materials and Methods

2.1. Data Acquisition System and Parameters

The data acquisition system comprised an all-fiber CWML system and a PTR-TOF-MS system. The experimental setup was installed on a 5.5 m long Iveco station wagon equipped with an operator's console and a power supply system. The system schematic diagram is shown in Figure 1.

2.1.1. All-Fiber Coherent Wind Measurement Lidar

In this study, we used a pulsed CWML system manufactured by Technovo Lidar High Tech Co., Ltd., Hefei, China (model KC-WL-2006 Lidar) [30]. The Lidar system is divided into two sub-systems: laser-transmitting system and laser-receiving system. In this study, the transmitting and receiving modules of telescope are integrated, which could be used to adjust focus. The seed laser produces a narrow linewidth laser with a wavelength of 1.55 μm. After beam amplification, collimation, and beam expansion, the laser is emitted into the atmosphere using a scanner at specific azimuth and elevation angles. Multiple laser "lines" are formed by rotational scanning, thus enabling 3D scanning of the detection area. The transmitted laser experiences Mie scattering in the atmosphere, and the receiving telescope receives the backward-scattered light. Next, the light received by telescope is collimated into parallel light through the optical fiber and reflecting telescope and then converted to photoelectric signal via balance detector. Finally, the data are collected by the acquisition card and stored in the computer. The whole system ensures the coordination of laser transmission and reception, data acquisition, and processing under the control

of the computer. The Lidar optical skylight was installed with special optical glass for mobile Lidar operations. The Lidar was placed on a special frame to keep the instrument stationary and reduce the impact of vehicle movement (see Figure 2). Specifically, the vehicle-mounted system hosted a CNS, which consisted of two high-precision GPS antenna, an accelerometer, and a gyroscope (see Figure 3). The first GPS (i.e., the Lidar GPS) was located on top of the Lidar special frame, while the second GPS (i.e., the vehicle GPS) was located on the bottom of vehicle structure, to enable the measurement of the vehicle and Lidar attitude.
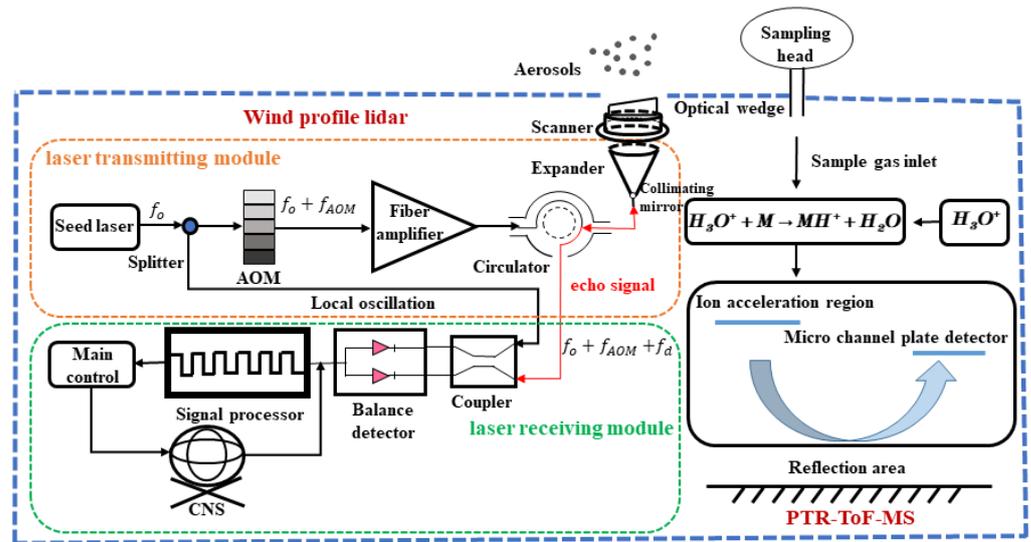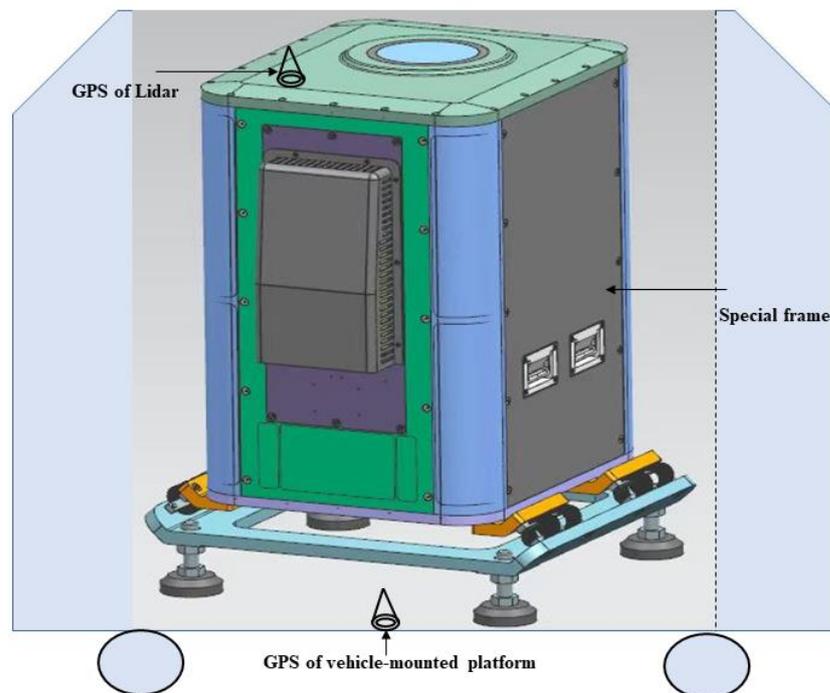

Figure 1. System schematic diagram.
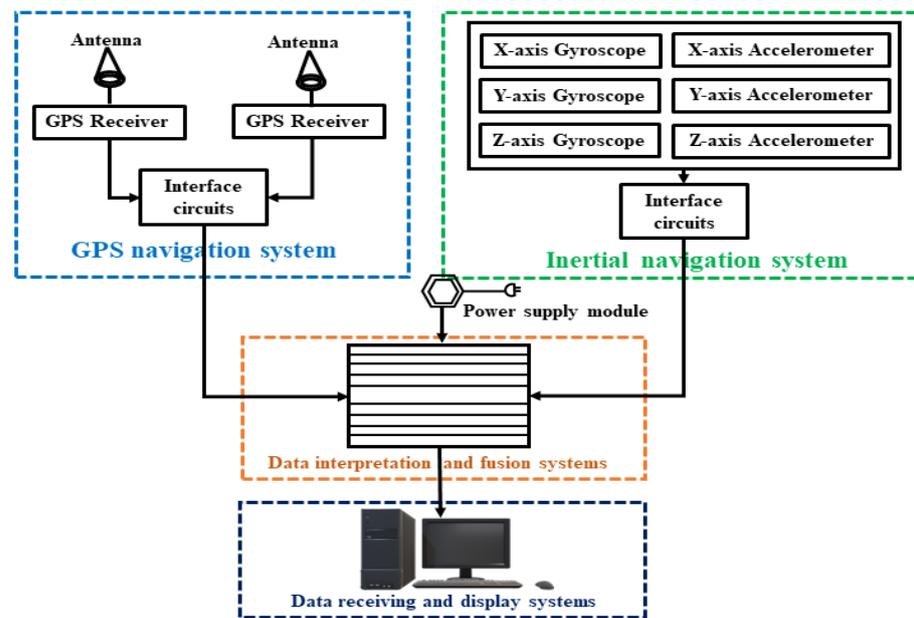

Figure 2. Special frame.

Figure 3. Combined navigation system.

The system is compact with a size of 835.0 mm × 550.5 mm × 888.6 mm, and mass of 50 kg. A laptop or PC is used to control the Lidar and store the measured data in each azimuth angle. Moreover, the laser emits a beam with 1.55 μm wavelength, where the pulse energy is 145 μJ. The single-pulse energy is limited. Noncoherent integration of echo signals is required. The spectral accumulation number is 20,000. The pulse width is τ = 400 ns, which corresponds to distance resolution of R = c × τ/2 = 60 m. The sampling frequency is f_s = 1 GHz, and N = 1024 points Fast Fourier Transform (FFT) is performed on this signal, so the spectral resolution f = fs/N = 0.98 MHz. To simplify the analysis, a valid section of echo signal power spectrum containing the peak value was intercepted for analysis, i.e., each range gate contained N_p = 112 valid points after the interception. In addition, the first 128 range gates were retained, i.e., 14,336 data were collected for subsequent analysis in each radial direction. The power spectrum data is shown in Figure 4 (only the first thirty range gates are shown). The X-coordinate represents frequency, the Y-coordinate represents range gate index, and Z-coordinate represents power spectral density (PSD). The first range gate stores noise data, and the second and third range gates store the mirror data. The mirror data are formed by the reflection and refraction phenomenon of the telescope system itself. The data in the 4th to the 128th range gates are valid data. The CNR is an important index used to detect the performance of Lidar. For a CWML system featuring a real-time signal processing function, the CNR is usually estimated from the average PSD data in the frequency domain. Moreover, the frequency-domain wideband CNR of the signal is defined as the ratio of the integration of signal PSD to the integration of noise PSD. As suggested by Manninen et al. [31], this study used a CNR of −20 dB as a threshold. After FFT, if the CNR of range gate is below the threshold, the data of range gate will be rejected. During experiments, the conical scanning is conducted with four lines of sight in a step-and-stare mode with a period of 10 s. The wedge scanner rotation speed was 180 degrees per second. The settling time was 2 s. The azimuth angle changed from 0° to 360°, with an angle step of 90°. Accordingly, the laser beams were pointed at four azimuths, north (0°), east (90°), south (180°), and west (270°), with an elevation angle of 60°. Many people were on duty in rotation. The vehicle-mounted Lidar operates at 30 km/h, ensuring at least two hours of detection time each morning, afternoon, and evening. The wind profile Lidar parameters are shown in Table 1.
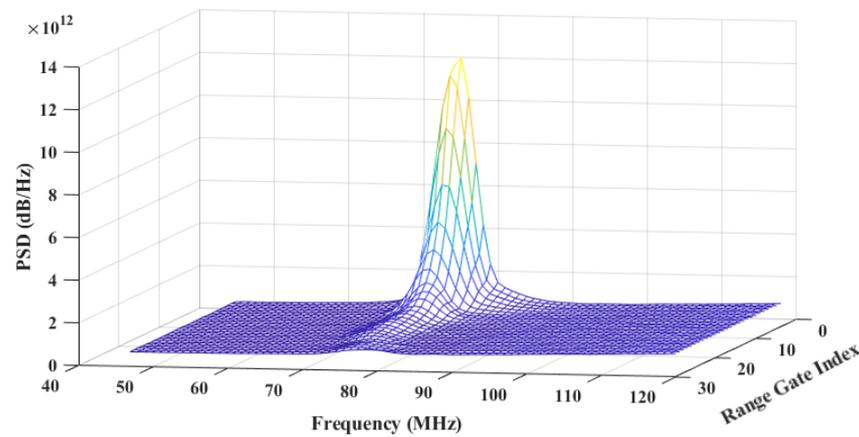
Figure 4. Raw power spectrum data.

Table 1. Coherent wind measurement Lidar system parameters.

Component	Qualification	Specification
Transmitter	Wavelength	1.55 μm
	Pulse energy	145 μJ
	Pulse repetition	10 kHz
	Pulse width	400 ns
	AOM frequency	80 MHz
Transceiver	Laser mode	Pulse
	Scan mode	Conical
	Elevation angle	60°
	Start angle	0°
	Step angle	90°
Data acquisition	Sampling frequency	1 GHz
	Sampling points	400
	Range resolution	60 m
	Blind range	60 m
	Gate number	128

2.1.2. Proton Transfer Reaction Time-of-Flight Mass Spectrometer

In addition to validating the vehicle-mounted CWML, we also detected the VOCs in navigation monitoring experiments. PTR-TOF-MS is the in situ sensor, and the sampling port of PTR-TOF-MS is located at the front end of the car roof to avoid the mis-sampling of the exhaust gases from the vehicle. The PTR-TOF-MS instrument used in this study consists of an ion source, a drift tube, and a mass spectrometer. The basic principle of PTR-TOF-MS relies on a proton-transfer reaction. To ensure the proton-transfer reaction required for ionization, the proton affinity (PA) of the VOC to be measured must be higher than that of water, i.e., $PA_{VOC} > PA_{H2O}$ (PA_{H2O} = 691 kJ/mol) must be satisfied [32]. Most VOCs possess a proton affinity higher than water, which is suitable for their ionization by H_3O^+. In addition, the major components of air [33] (such as oxygen, nitrogen, and carbon dioxide) have a proton affinity lower than water. Hence, they are not ionized, which does not affect target detection. In PTR-TOF-MS, the water vapor discharge from the ion source generates the active ion H_3O^+. The sampling port introduces the ambient air into the drift tube, where the air undergoes a proton-transfer reaction with the reagent ion H_3O^+ [34].

$$H_3O^+ + R \rightarrow RH^+ + H_2O, \tag{1}$$

where R is the VOC molecule to be measured, and RH^+ is the production. The count rates cps (H_3O^+) and cps (RH^+) of H_3O^+ and RH^+ were measured by the mass detector, and the absolute concentrations of R were deduced as follows:

$$[R] = \frac{[RH^+]}{[H_3O^+]_0} \times \frac{1}{kt} = \frac{cps(RH^+)}{cps(H_3O^+)} \times \frac{1}{kt}, \tag{2}$$

where [R] represents the absolute concentration of the substance R to be measured, $[H_3O^+]_0$ is the initial concentration of H_3O^+, k is the rate constant for the protonation reaction, and t is the average time for the ion to pass through the reaction zone.

2.2. Motion Compensation

2.2.1. Defining the Three-Dimensional Coordinate System

In this study, a new CNS was equipped to measure and provide the running speed and attitude angle data at any time during the navigation monitoring experiments for real-time correction of the errors [29]. After the signal processing module processes these data, the line of sight is corrected in real time. The dual GPS difference is used to determine the attitude angle data of the vehicle-mounted platform, and the average of the motion velocities measured by the dual GPS is used as the motion velocity of the vehicle-mounted platform. When one of the GPS signals fails to be received, it is supplemented by observations from the INS, which are fed into the algorithm as measurements of the motion error. To describe the vehicle-mounted system, we define the right-handed Cartesian XYZ moving coordinate system (referred to as the M-system) of the vehicle-mounted platform and the north–east–down right-handed Cartesian NED fixed global frame of reference (referred to as the F-system) (see Figure 5). In addition, we also define the right-handed Cartesian MNP antenna coordinate system (referred to as the A-system). The origin of coordinates is defined as the antenna center, M-axis is along the optical axis of the radar antenna, and the N-axis is perpendicular to the M-axis. In real operating conditions of CWML, external forces cause a translational motion in the N, E, and D directions (surge, sway, and heave, respectively) and a rotational motion along the N, E, and D axes (roll, pitch, and yaw, respectively) [35]. The changes in running speed and attitude angle of the vehicle platform are represented by the four parameters: real-time operating speed, roll, pitch, and yaw. Moreover, motion compensation (MC) is divided into two parts: attitude compensation [36] and speed compensation [37].
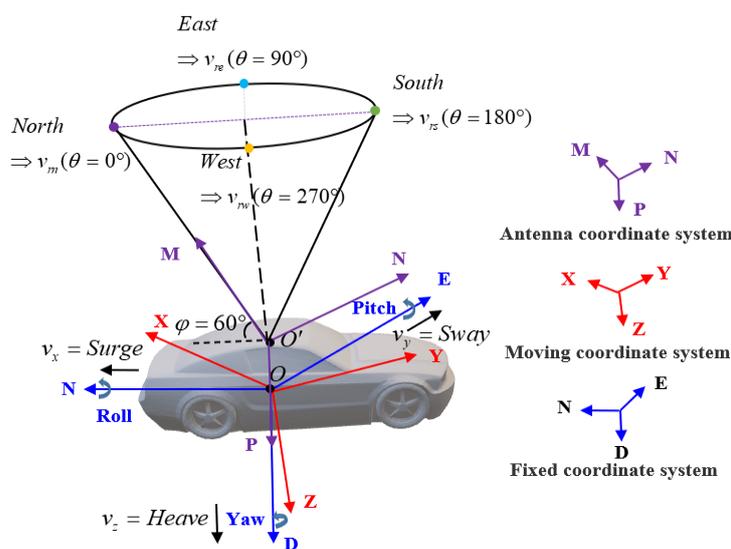

Figure 5. Schematic diagram of four-beam CWML.

2.2.2. Attitude Compensation

Attitude compensation is achieved by calculating the attitude matrix in real time using the attitude angle measured by the CNS. According to the definition of attitude angle, the transformation matrix from M-system to F-system is given as

$$C_M^F = \begin{bmatrix} \cos\alpha\cos\gamma + \sin\alpha\sin\beta\sin\gamma & \sin\alpha\cos\beta & \cos\alpha\sin\gamma - \sin\alpha\sin\beta\cos\gamma \\ \cos\alpha\sin\beta\sin\gamma - \sin\alpha\cos\gamma & \cos\beta\cos\alpha & -\sin\alpha\sin\gamma - \cos\alpha\sin\beta\cos\gamma \\ -\cos\beta\sin\gamma & \sin\beta & \cos\beta\cos\gamma \end{bmatrix}, \quad (3)$$

where α, β, and γ are the yaw, pitch, and roll angles observed by the INS, respectively. An azimuthal relationship between the M-system and F-system describes the attitude of the vehicle platform. Moreover, the methods to describe the azimuthal relationship between the two coordinate systems include the three-parameter method (Euler's angle method), the four-parameter method (quaternion method), and the nine-parameter method (directional cosine method) [37]. In this paper, the quaternion method is used to describe the rotational information in a three-dimensional space and solve the attitude transformation matrix. The quaternions of rotation of the M-system relative to the F-system are

$$Q = q_0 + q_1 \vec{x} + q_2 \vec{y} + q_3 \vec{z}, \quad (4)$$

where q_0, q_1, q_2, and q_3 are real numbers, and $\vec{x}$, $\vec{y}$, and $\vec{z}$ are mutually orthogonal unit vectors. Then, the quaternion expression of the angular velocity vector of the M-system relative to the F-system is given as

$$\vec{\omega}_M^F = 0 + \omega_{Fx}\vec{x} + \omega_{Fy}\vec{y} + \omega_{Fz}\vec{z}, \quad (5)$$

where ω_{Fx}, ω_{Fy}, and ω_{Fz} are the angular velocity vectors along the N, E, and D axes, respectively. The real-time correction of Q is implemented using the quaternion differential equation, which corresponds to a matrix of the form

$$\begin{bmatrix} \dot{q}_0 \\ \dot{q}_1 \\ \dot{q}_2 \\ \dot{q}_3 \end{bmatrix} = \frac{1}{2} \begin{bmatrix} 0 & -\omega_{Fx} & -\omega_{Fy} & -\omega_{Fz} \\ \omega_{Fx} & 0 & \omega_{Fz} & -\omega_{Fy} \\ \omega_{Fy} & -\omega_{Fz} & 0 & \omega_{Fx} \\ \omega_{Fz} & \omega_{Fy} & -\omega_{Fx} & 0 \end{bmatrix} \begin{bmatrix} q_0 \\ q_1 \\ q_2 \\ q_3 \end{bmatrix}, \quad (6)$$

Similarly, the quaternion expression of the angular velocity vector of the A-system relative to the M-system is

$$\vec{\omega}_A^M = 0 + \omega_{Mx}\vec{x} + \omega_{My}\vec{y} + \omega_{Mz}\vec{z}, \quad (7)$$

where ω_{Mx}, ω_{My}, and ω_{Mz} are the angular velocity vectors along X, Y, and Z axes, respectively. Next, the angular velocity of the A-system relative to the F-system can be expressed as

$$\vec{\omega}_A^F = \vec{\omega}_M^F + \vec{\omega}_A^M, \quad (8)$$

In addition, the attitude matrix in quaternion form can be expressed as

$$C = \begin{bmatrix} q_0^2 + q_1^2 - q_2^2 - q_3^2 & 2(q_1q_2 - q_0q_3) & 2(q_1q_3 + q_0q_2) \\ 2(q_1q_2 + q_0q_3) & q_0^2 + q_1^2 + q_2^2 - q_3^2 & 2(q_2q_3 - q_0q_1) \\ 2(q_1q_3 - q_0q_2) & 2(q_2q_3 + q_0q_1) & q_0^2 - q_1^2 - q_2^2 + q_3^2 \end{bmatrix}, \quad (9)$$

The flowchart of the attitude compensation algorithm is shown in Figure 6. Firstly, the attitude angle measured by GPS/INS is substituted into a transformation matrix to obtain the attitude matrix of the M-system relative to the F-system. Here, the elements in the matrix are functions of yaw angle, roll angle, and pitch angle. Next, the attitude matrix is normalized by using the quaternion method. Progressively, the attitude matrix of the

A-system relative to the F-system is derived from the azimuth and elevation of the antenna beam, where the elements of the matrix are functions of azimuth and elevation angles. In this way, the attitude matrix of the A-system relative to the F-system is obtained. Finally, the antenna beam's actual azimuth angle and elevation angle are obtained by comparing the azimuth and elevation of the two adjacent moments. The advantages of the above attitude compensation algorithm are, on the one hand, the attitude and orientation data of the vehicle platform observed by the CNS are input to the signal processing system in real time; on the other hand, the algorithm as an algorithm module can be integrated into the signal processing system without the influence of any mechanical equipment, which is more efficient and stable compared to the adjustment platform of the antenna.
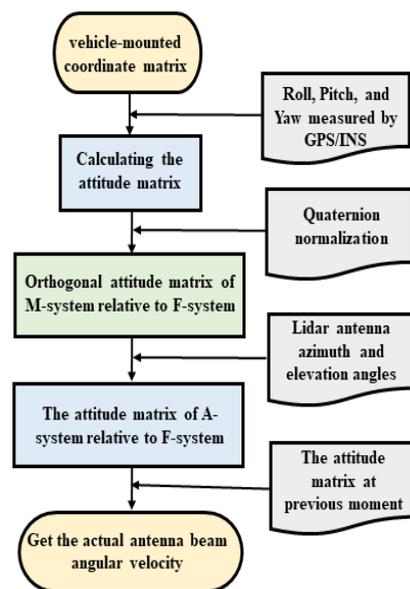

Figure 6. Flowchart of attitude compensation.

2.2.3. Speed Compensation

If the vehicle-mounted platform maintains a uniform speed in the horizontal direction, i.e., the platform has zero acceleration in all directions, then the motion speed compensation is a constant, i.e., only the effect of the vehicle's linear motion needs to be considered during the driving process. However, since it is difficult for the vehicle to maintain a uniform speed, a motion speed compensation algorithm is introduced in the actual driving process [38].

$$V_r = V_T - V_R, \tag{10}$$

where V_r is the radial velocity of the aerosol particles relative to the radar antenna, which is also the actual radial velocity measured by the Lidar antenna. Meanwhile, V_T is the radial velocity of the aerosol particles relative to the F-system, and V_R is the radial velocity of the A-system relative to the F-system. Obviously, the accurate acquisition of V_T is necessary for obtaining V_R's accurate and reliable value.

The corresponding algorithm flowchart is shown in Figure 7. Initially, the running speed of the vehicle-mounted platform is measured in the F-system using the CNS. Moreover, the azimuth and elevation of the radar antenna relative to the M-system are obtained from the observation data. The radial running speed of the vehicle platform is calculated based on the speed, azimuth angle, and elevation angle. Then, the aerosol particles' radial speed and relative distance are obtained from the observed data. Furthermore, the actual radial speed of the aerosol particle is calculated, and the actual position of the aerosol particle and the angle matrix along the three axes are calculated in the F-system by coordinate transformation. Finally, the speed of aerosol particles along three coordinate axes is obtained in the F-system.
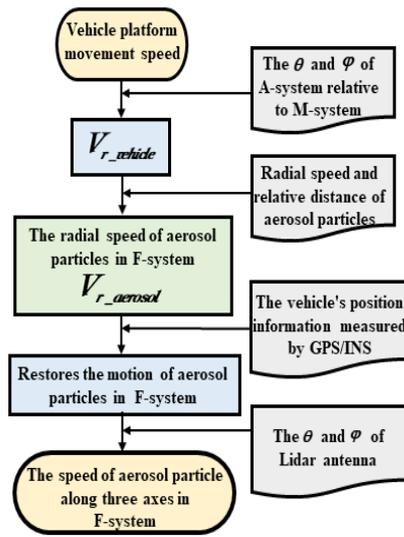
Figure 7. Flowchart of speed compensation.

2.3. Spectral Signal Processing

2.3.1. Data Pre-Processing

Suppression of the base noise plays an essential role in the spectral processing of CWML to accurately estimate the radial wind speed. If the base noise is ideally white and has a known average level, it is easy to reduce. However, the base noise is colored due to the frequency gain characteristics of the electrical receiver circuit. In addition, the average noise level varies according to the scattered noise level. Empirically, the scattered noise level constantly fluctuates, as the base noise can quickly fluctuate depending on the ambient temperature. In our processing, the CWML recorded the noise spectrum without any received signal when the laser was stopped and subtracted the noise spectrum from the received signal spectrum. For each range gate signal, the base noise signal was subtracted (counterpoint subtraction) and the mean value of the base noise was added, and the resulting spectrum is a flat-base spectrum, as shown in Figure 8. This process whitens the base noise and helps the correct signal peak to be detected. Subsequently, the spectra were smoothed according to the method proposed by Lin et al. for estimating radial wind from smoothed accumulated spectra [39]. Examples of intermediate results are shown in Figure 9.
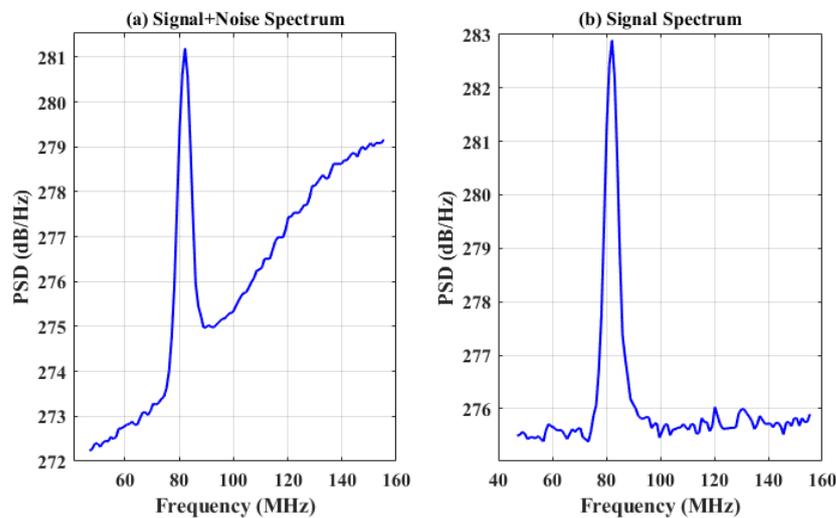

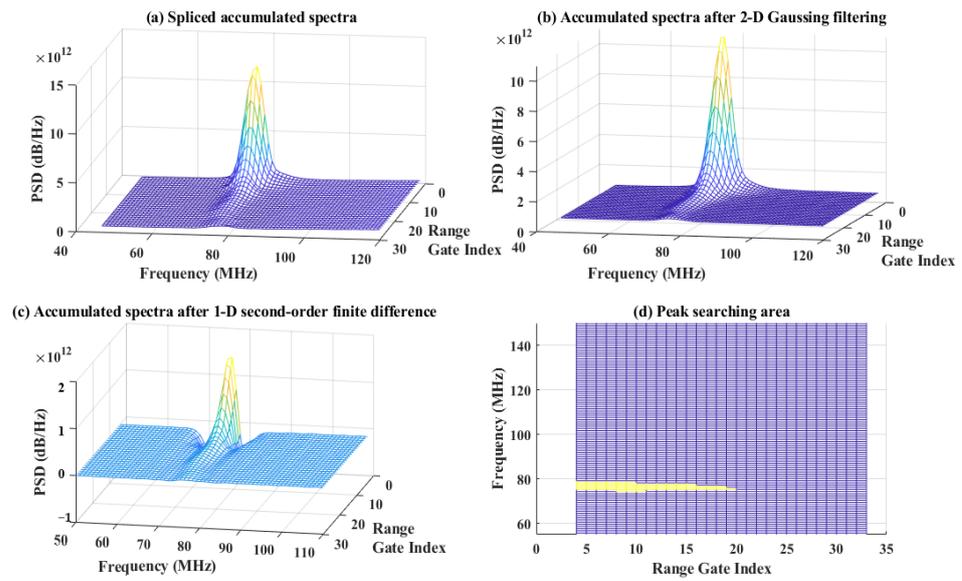**Figure 8.** Schematic of base noise reduction.

Figure 9. Example results of accumulated spectrum estimation.

2.3.2. Automatic Peak-Finding Algorithm

The Doppler shift caused by the motion of the scatterer is determined by identifying the highest value in the power spectrum of the echo signal. According to the characteristics of the power spectrum of echo signal, a method of automatically retrieving peak value is proposed. The flowchart of the automatic peak-finding algorithm (APFA) is shown in Figure 10.
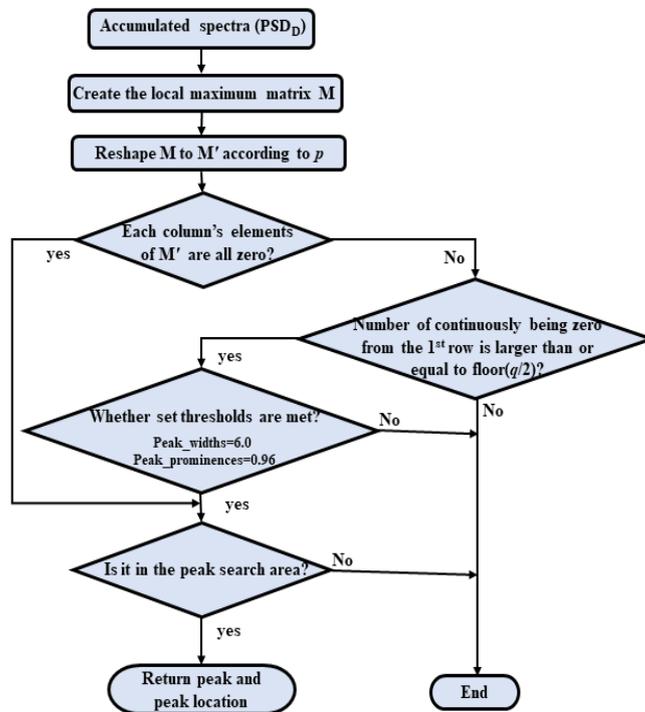

Figure 10. Flowchart of adaptive local peak-retrieval algorithm.

Firstly, based on the Automatic Multiscale-Based Peak Detection (AMPD) method [40], the local maximum matrix M ($m \times n$) of the data sequence is established, where m = floor $(n/2) - 1$, n = 14,336.

$$M = \begin{bmatrix} m_{11} & m_{12} & \cdots & m_{1n} \\ m_{21} & m_{21} & \cdots & m_{2n} \\ \vdots & \vdots & \ddots & \vdots \\ m_{m1} & m_{m2} & \cdots & m_{mn} \end{bmatrix} = (m_{i,j}), \tag{11}$$

Secondly, the local maximum dimension of M should be controlled. The distribution of the 0 elements in the row vectors in the M matrix indicates the number of local maxima of the sequence within the moving window. The number of 0 elements in all row vectors in the M matrix is counted and the row with the greatest number of 0 elements is found, denoted as p (p = max [sum ($m_{i,j}$ = 0)]). The matrix M is reshaped by deleting row vectors with row $i > p$ to form a new matrix M' ($p \times n$).

Thirdly, peak positioning and compensation are performed. When all the elements of a column are zero, the element in the data series corresponding to that column is a candidate peak point. In addition, if a data point follows the trend of the left-hand proximity rising and the right-hand proximity falling within a certain window, it also needs to be classified as a peak point. If the corresponding new matrix M' column vector satisfies (1) the first element of the column vector is 0; (2) the number of consecutive 0 elements from the first row $H \geq$ floor $(q/2)$; and (3) the candidate peak point satisfies the threshold condition, then the data point is added within the candidate peak point.

Finally, peaks that are not in the peak-searching area are filtered out, and the peak-searching area is shown in the yellow area in Figure 9d.

The first few range gates store the noise and mirror data, which should be removed after the peak search. The results of adaptive local peak retrieval of the measured power spectrum are given in Figure 11. The red asterisk represents the result of the peak search at each range gate. The horizontal coordinate represents the iteration of the set of frequencies in the spectrum with a sampling frequency of 1 GHz. Notably, the amplitude of the echo signal becomes increasingly faint as the detection distance increases, with the signal gradually being drowned out by noise at around 30 range gates (the corresponding sampling point is 3360). Therefore, the horizontal axis stopped at 3500. Vertical coordinate (PSD) is the result of a logarithmic operation on the sampling data to facilitate observation of the peak-finding results. The formula for logarithmic functions is y' = 10 × log$_{10}$(y), where y is the vertical coordinate data in Figure 9, and y' is the vertical coordinate data in Figure 11. Figure 11a shows the raw accumulated spectrum without spectra splicing. Circled in the diagram's red rectangular box is the signal drowned out by the noise; Figure 11b shows the peak-finding results, i.e., further processing in Figure 9d, with the red asterisks indicating the peak-finding results at each range gate. The APFA algorithm has the advantage of a low probability of false peaks and a strong identification of weak peaks, providing a fast, accurate, and adaptive method for the online analysis of CWML in the field.

2.3.3. Wind Field Retrieval

The estimation of radial wind from the power spectrum is based on wind spatial continuity [37]. The distance resolution between adjacent distance gates is smaller than the scale of most wind shear [41]. The measurement is approximately valid during the time needed to measure along the four lines of sight. Radial wind can be estimated by the Doppler principle. According to the principle of Doppler frequency shift, the echo signal received by the telescope through the atmosphere will generate a frequency shift with respect to the signal transmitted by the telescope [42]. Fundamentally, the relationship between Doppler frequency shift and radial wind speed can be described as follows [43]:

$$f_d = f_r - f_0 = (2V \cos \theta_0)/\lambda, \tag{12}$$

where f_r is the frequency of echo signal, f_0 is the frequency of output laser, θ_0 is the included angle between emitting laser and motion direction of the particle to be measured, λ is the central wavelength of the emitting laser, and V is the movement speed of the particle. Accordingly, CWML can measure the radial wind field information by detecting the Doppler frequency shift in the echo signal. Moreover, the four-beam scanning mode is demonstrated in Figure 5. Here, the zenith angle of laser emission is φ, and the radial wind fields with azimuth angles of $0°$, $90°$, $180°$, and $270°$ are measured successively. The radial wind speeds in the four measurement directions are as follows [18]:

$$V_{rn} = V_y \sin \varphi + V_z \cos \varphi, \tag{13}$$

$$V_{re} = V_x \sin \varphi + V_z \cos \varphi \tag{14}$$

$$V_{rs} = -V_y \sin \varphi + V_z \cos \varphi \tag{15}$$

$$V_{rw} = -V_x \sin \varphi + V_z \cos \varphi \tag{16}$$

Then, V_x, V_y, and V_z are given as

$$V_x = (V_{re} - V_{rw})/2 \sin \varphi, \tag{17}$$

$$V_y = (V_{rn} - V_{rs})/2 \sin \varphi \tag{18}$$

$$V_z = (V_{re} + V_{rw} + V_{rn} + V_{rs})/4 \cos \varphi \tag{19}$$

Additionally, the magnitude and direction of horizontal wind speed are

$$V_h = [(V_{re} - V_{rw})^2 + (V_{rn} - V_{rs})^2]^{1/2}/(2 \sin \varphi), \tag{20}$$

$$\gamma = \arctan(V_x/V_y) + \pi\{1 - sign[(V_y + |V_y|) \cdot V_x\}, V_y \neq 0 \tag{21}$$
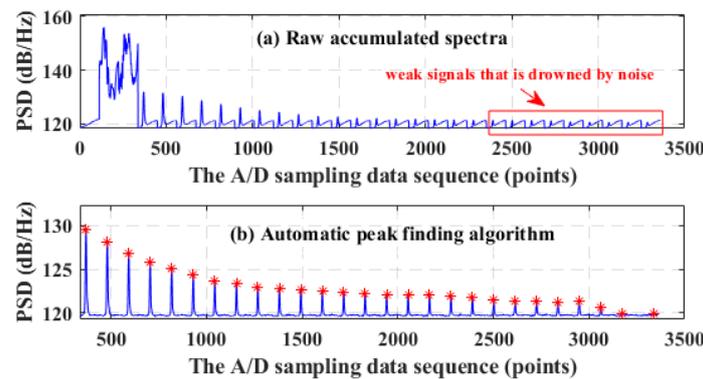

Figure 11. Adaptive local peak-retrieval results of the measured power spectrum.

3. Results and Discussion

3.1. Sampling Sites and Sample Collection

The field experiment was performed in Hefei, Anhui Province, China (117.12°E, 31.85°N), from 29 July to 5 August 2021. To verify the feasibility of applying CWML to vehicles, calibration experiments, comparison experiments, and continuous observation experiments were carried out successively. According to the characteristics of Hefei In-

novation and Entrepreneurship Industrial Park (IEIP), three distinct sampling sites were selected, including the residential district (RA), commercial district (CD), and industrial park (IP). These sites are representative of the different atmospheric wind field data, and reflect Hefei's overall three-dimensional wind field information. The RA site is located west of IEIP, surrounded by residential buildings with substantial forested areas and low industrial activity. Likewise, the CD site represents the mixed emissions of commercial activities and vehicle exhaust. In contrast, the IP site is far from the IEIP, where the industrial activity likely strongly affects air quality.

3.2. Calibration Test

In this study, calibration tests in the static state for both vehicle-mounted CWML and a reference Lidar (the fixed Lidar) were carried out. The Lidars were set to simultaneously measure the wind field under static conditions. The reference Lidar (KC-WL-2004) has the same specifications as those of the KC-WL-2006. The reference Lidar (KC-WL-2004) was verified through a verification test with a radiosonde. In addition, the calibration experimental site was selected on the roof of block C4 in the Innovation Industrial Park (117.12°E, 31.85°N). The two Lidars were kept five meters apart to ensure identical measurements on a 30 min time basis (see Figure 12). Vertical wind profiles were observed for 24 h from 00:00 on 29 July to 00:00 on 30 July in 2021, to study the stability of the vehicle-mounted CWML system.

Figure 12. Calibration test.

Figure 13 shows the wind profiles measured by the KC-WL-2006 Lidar and the reference Lidar in the horizontal direction during the calibration test. The maximum values of the standard deviation of magnitude and the direction of horizontal wind speed measured using two instruments were 0.58 m/s and 3.29°, with average values of 0.26 m/s and 1.41°, respectively. The calibration results of wind direction and speed exhibit good consistency in the detection distance. In low-altitude measurement, wind speed and direction near the ground are affected by terrain, which induces certain differences. Alternatively, with increasing detection height (more than 2500 m), the energy of backscattering signals received by the two Lidars decreases, thereby increasing the measurement errors for wind speed and direction. The main purpose of this experiment was to verify the stability of KC-WL-2006 Lidar before the formal vehicle-mounted experiment and in preparation for navigation monitoring.
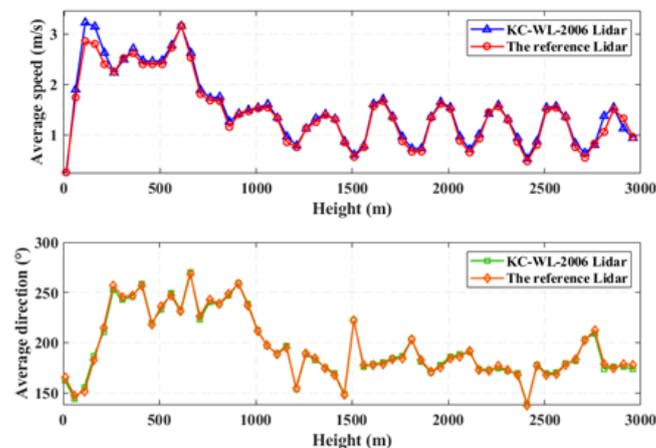
Figure 13. Average speed and direction measured by the KC-WL-2006 Lidar and the reference Lidar.

3.3. Contrasting Observations

A small-range navigation monitoring test was carried out after the calibration test. In the actual operating conditions of CWML, a vehicle's traveling motion disturbs the conical scan, where the rotational and translational motion influence the pointing direction and measured radial velocities. Therefore, the CNS is equipped during the navigation monitoring test for the real-time correction of the errors caused by vehicle movement. As shown in Figure 14, the solid orange line represents the running trajectory of the vehicle-mounted platform, while the orange arrow represents its driving direction. Moreover, the direction of the wind profile arrow indicates the wind direction, and the arrow's color indicates the wind speed. During the contrasting observation experiment, the maximum distance between the two Lidars was less than 1.5 km, and the average distance between the two Lidars was about 600 m. The fixed Lidar was set up in a stand-still configuration on the roof of block C4 in the Innovation Industrial Park (117.12°E, 31.85°N) as a reference device. Contrast observations for both vehicle-mounted CWML and a reference fixed Lidar were carried out from 00:00 to 24:00 on 1 August to verify the wind field measurement ability of the vehicle-mounted Lidar.
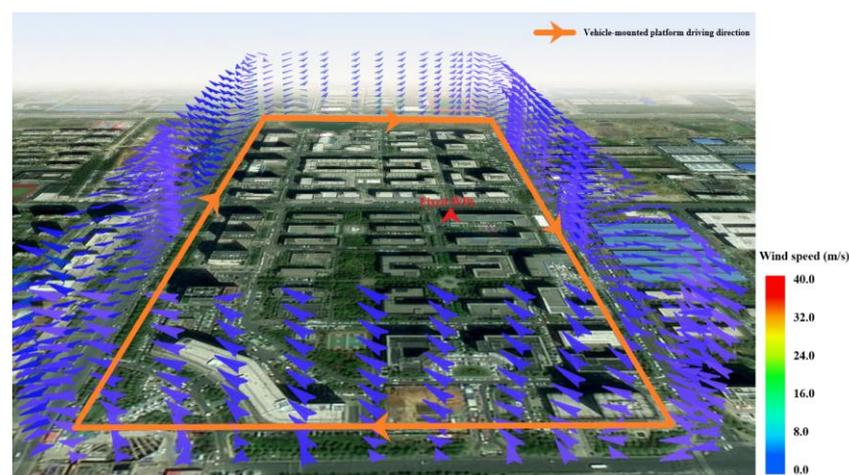

Figure 14. Wind plume chart measured by the vehicle-mounted Lidar.

To demonstrate the performance and advantages of APFA and MC, we evaluated the following two criteria. The first was the root mean square of the difference (RMSD)

between the vehicle-mounted Lidar (V_{VM}) and the reference Lidar (V_R) to evaluate the biases of wind vector estimations:

$$\text{RMSD} = \sqrt{\text{mean}(|V_{VM} - V_R|_2)}, \tag{22}$$

The second criterion was the proportion of good vector estimates (PGE), where the $|V_{VM} - V_R| < 2.5$ m/s was chosen as the threshold. As shown in Figure 15 "Before APFA and MC" refers to the processing results of the accumulated spectra mentioned in Section 2 without applying APFA and MC. Similarly, "After APFA" refers to the processing results after applying the APFA. "After MC" refers to the processing results after applying the MC. "After APFA and MC" indicates the processing results after applying APFA and MC. It can be seen from Figure 15a that the RMSDs of the estimated wind vector increased gradually with the increase in detection distance. The application of APFA plays a vital role in the wind vector estimation process, increasing the detection distance by about 500 m. The effective detection height of Lidar could reach 3 km. Furthermore, the vibration of the vehicle platform interferes with the cone scan, resulting in a broadening of the spectrum and confusion in the beam pointing. Here, the application of motion compensation dramatically improved the detection accuracy and detection distance. The case "After APFA and MC" achieved the best result, where the RMSD remains at a low level. Meanwhile, "After APFA and MC" is also the best for PGE (see Figure 15b). Notably, the PGE of the "Before APFA and MC" dropped to 90% at the 17th range gate. Evidently, "After APFA" performed better than "Before APFA and MC", and its PGE dropped to 90% at the 23rd range gate. In addition, the PGE of "After MC" method dropped to 90% at the 43rd range gate. Thus, APFA and MC are proven to be effective for Lidar on a moving platform.
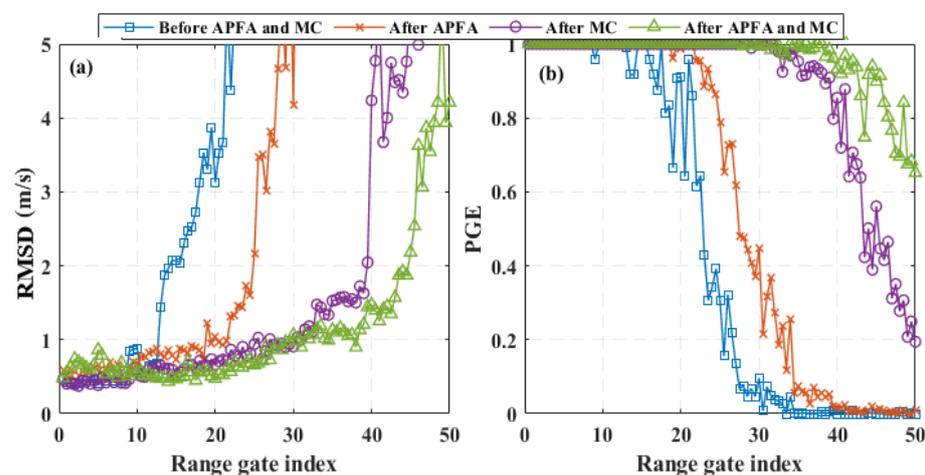

Figure 15. Evaluation results: (**a**) the root mean square of the difference; (**b**) the proportion of good vector estimates.

As illustrated in Figure 16, the average wind speed and wind direction measured by the KC-WL-2006 Lidar and the vehicle-mounted Lidar exhibit good consistency. Furthermore, the correlation coefficients of the magnitude and direction of horizontal wind speed measured using two instruments were 0.94 and 0.91, respectively. Moreover, the maximum values of the standard deviation of the magnitude and direction of horizontal wind speed measured using two instruments were 1.05 m/s and 9.86°, with average values of 0.58 m/s and 4.20°, respectively. These errors include vehicle movement errors, system measurement errors, and atmospheric variations during the 30 min measurement period. The vehicle-mounted Lidar moves around the fixed Lidar, and the distance between the two Lidars changes as the motion platform moves. Thus, compared with the trends observed in the comparative test, the trends of the wind profiles measured by the two Lidars in the calibration test are more consistent. Additionally, the correlation between the results of

the two Lidars at different detection heights was analyzed. Figure 17 shows the scatter plots and the corresponding linear regressions (red circles and lines) of the wind speed and wind direction data measured by the vehicle-mounted Lidar and the reference Lidar. The deviations in wind speed and wind direction between the two Lidars are also shown (blue triangles). Where (a), (b), and (c) are the wind speed measurement deviations at 500, 1000, and 2000 m, respectively, (d), (e), and (f) are the wind direction measurement deviations at 500, 1000 and 2000 m, respectively. The Lidar gives an average set of data every half hour during the day's comparison time. Thus, 48 data points are given to participate in the fit at the same detection height. The RMSEs of the wind speed and wind direction measurements gradually increase with the increase in detection distance. Even at a detection distance of 2000 m, the RMSEs of wind speed and direction are 0.76 and 8.46, respectively. The R-Square measures the model fit, and the closer its value is to 1, the better the model fit is. As can be seen from Figure 17, the R-Square of wind speed changes from 0.97 to 0.82, while that of wind direction changes from 0.99 to 0.98. The good consistency of wind speed and wind direction measured by the two Lidars also reflects the effective performance of the APFA and MC applied to the vehicle-mounted Lidar.
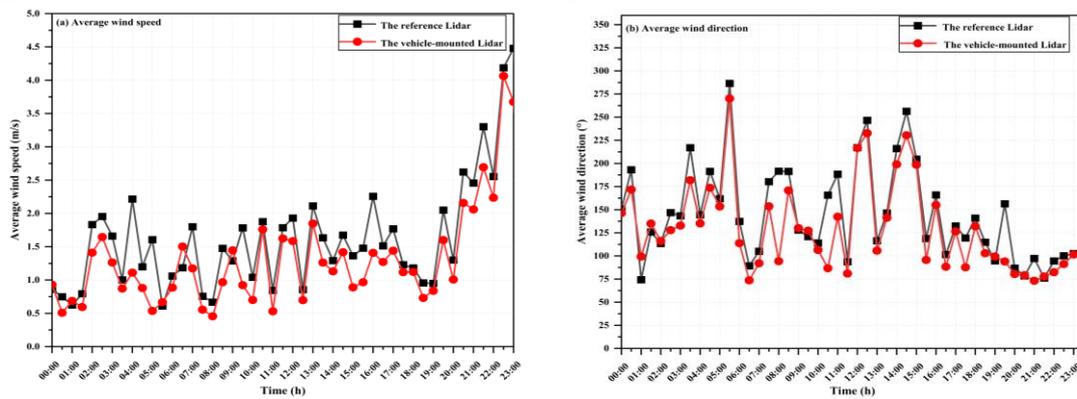

Figure 16. Results measured by the reference Lidar and the vehicle-mounted Lidar.
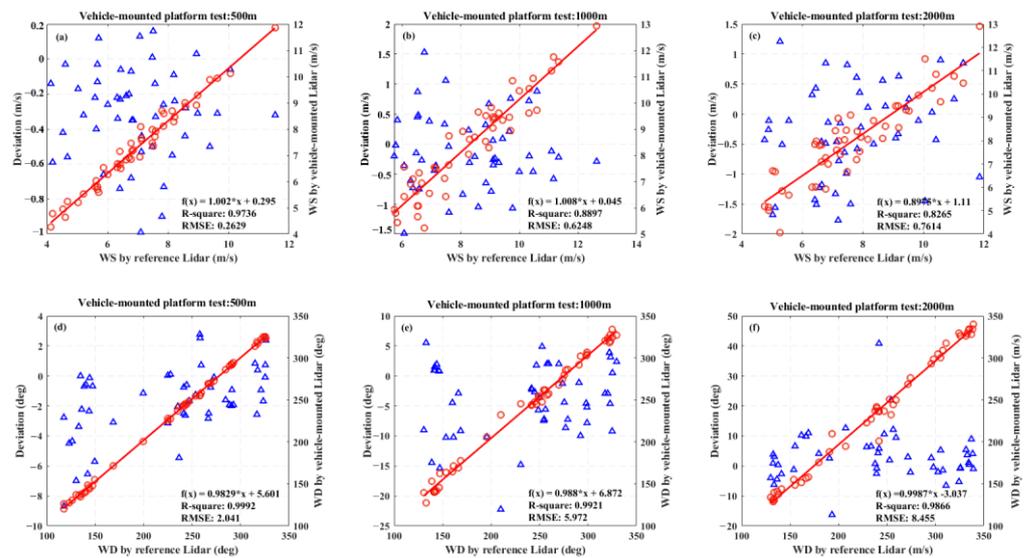

Figure 17. Comparison of the wind speed (WS) and wind direction (WD) data retrieved by the vehicle-mounted Lidar and the reference Lidar during the navigation monitoring: (**a**) wind seed measurement deviations at 500 m; (**b**) wind seed measurement deviations at 1000 m; (**c**) wind seed measurement deviations at 2000 m; (**d**) wind direction measurement deviations at 500 m; (**e**) wind direction measurement deviations at 1000 m; (**f**) wind direction measurement deviations at 2000 m.

3.4. Continuous Observation Experiment

A three-day continuous observation experiment was conducted on vehicle-mounted wind Lidar from 3 August to 5 August 2021. To understand the role of wind fields in energy and material transport, concentrations of different groups of VOCs were detected using PTR-TOF-MS at three sampling sites simultaneously. The navigation vehicle was equipped with temperature and humidity sensors to extract the temperature and humidity information in real time. During the three days, 2719 wind data points were collected. Among these, 484 points were discarded due to vehicle movement, unsuitable wind direction relative to the vehicle's heading, or some technical problem associated with the data acquisition.

3.4.1. Characteristics of Atmospheric Wind Fields in Different Functional Areas

In order to understand the atmospheric wind field conditions in the Hefei Economic Development Zone and the surrounding areas, a three-day navigation observation experiment was conducted from 3 August to 5 August 2021 to obtain the spatial and temporal distribution of the atmospheric wind field. The effectiveness of this vehicle-mounted Lidar in regional atmospheric wind field detection was verified. Figure 18 shows the wind plume maps obtained from the Lidar at the three sampling points. The direction of the wind profile arrow indicates the wind direction, and the arrow's color indicates the wind speed. Figure 18a illustrates a two-hour extensive navigation survey conducted at the RA site from 9 a.m. to 11 a.m. on 4 August. The average temperature of the environment was 29°, the average humidity was 70%, the wind direction was towards the east, and the wind speed was at level 2. The wind speed and humidity near Shushan Lake were significantly higher than the other areas, with humidity levels as high as 78%. Moreover, the wind field navigation monitoring at the CD site is shown in Figure 18b. The missing area of wind profile in Figure 18 was caused by the shielding of buildings during laser cone scanning. Additionally, Figure 18c shows the navigation monitoring of the IP site. Due to the variability in the atmospheric environment at the IP site, we chose to monitor at several times on 5 August. During monitoring, the temperature was about 33 °C, the humidity was about 65~93%, the wind direction was easterly, and the wind speed was level 2.
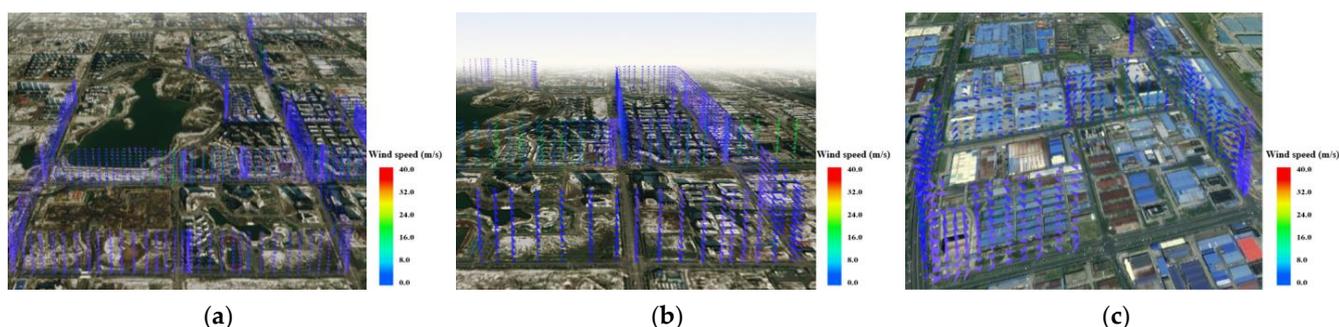

| (a) | (b) | (c) |

Figure 18. Navigation monitoring results: (**a**) the RA site navigation monitoring; (**b**) the CD site navigation monitoring; (**c**) the IP site navigation monitoring.

A wind-dominated pollutant transport process was observed during the IP site navigation monitoring, and Figure 19 reflects the variation in the wind field at different moments during the period. Figure 19a,b show the grey-scale plots of wind speed and wind direction as a function of time and height, respectively, obtained from CWML measurements on August 5 during the navigation monitoring, with the horizontal coordinates indicating time and the vertical coordinates indicating height. The shades of color in Figure 19a represent the wind speed magnitude, and the shades of color in Figure 19b indicate the wind direction, where 0° represents a northerly wind, 90° represents an easterly wind, 180° represents a southerly wind, and 270° represents a westerly wind. Accordingly, Figure 20 shows the wind speed and direction results measured at the local ground-based weather vertical coor-

dinates indicating height. The wind plume represents the magnitude of horizontal wind speed, and the wind direction bar indicates the horizontal wind direction. The atmospheric wind field changes significantly with increasing height, and a more pronounced weather evolution can be seen more clearly in Figure 20. At the beginning of the experiment, the dominant wind direction was predominantly south-westerly, associated with the Hefei area being influenced by cold air moving south from the middle and high latitudes in summer. Later, possibly influenced by warm moist air from the tropical ocean moving northwards, the wind direction above 1 km shifted to southeasterly after 4 am, with significant wind shear. In this region, warm air meets cold air coming in from the south and forms a front at the junction. Evidently, the wind field changed dramatically at a low altitude of 1000 m, with local high wind values appearing at 4 a.m. and 6 a.m. After 3 p.m., the wind speed decreased significantly and remained basically less than 5 m/s.
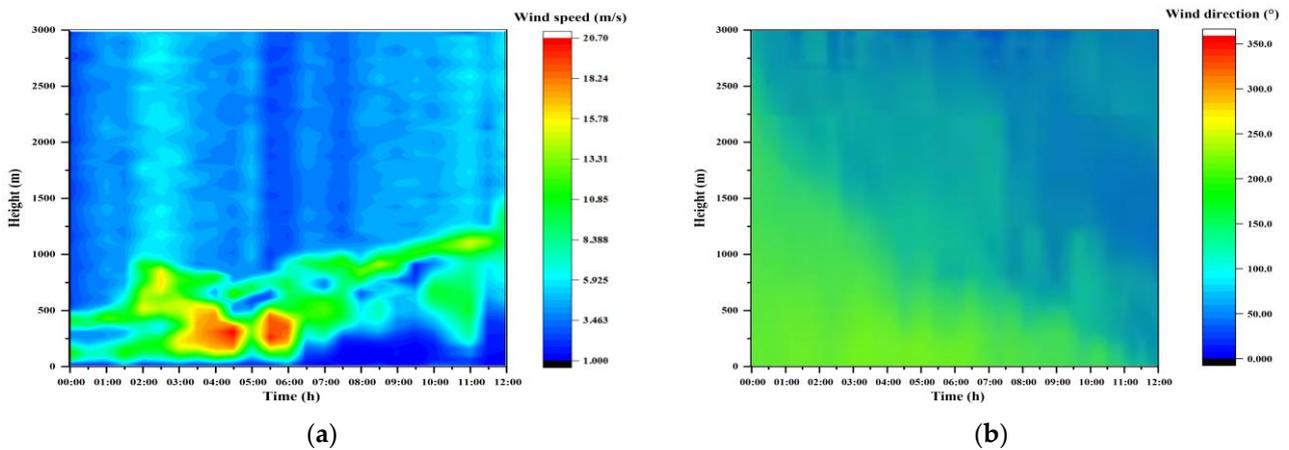

(a)   (b)

Figure 19. The IP site navigation monitoring wind profile: (**a**) wind speed; (**b**) wind direction.
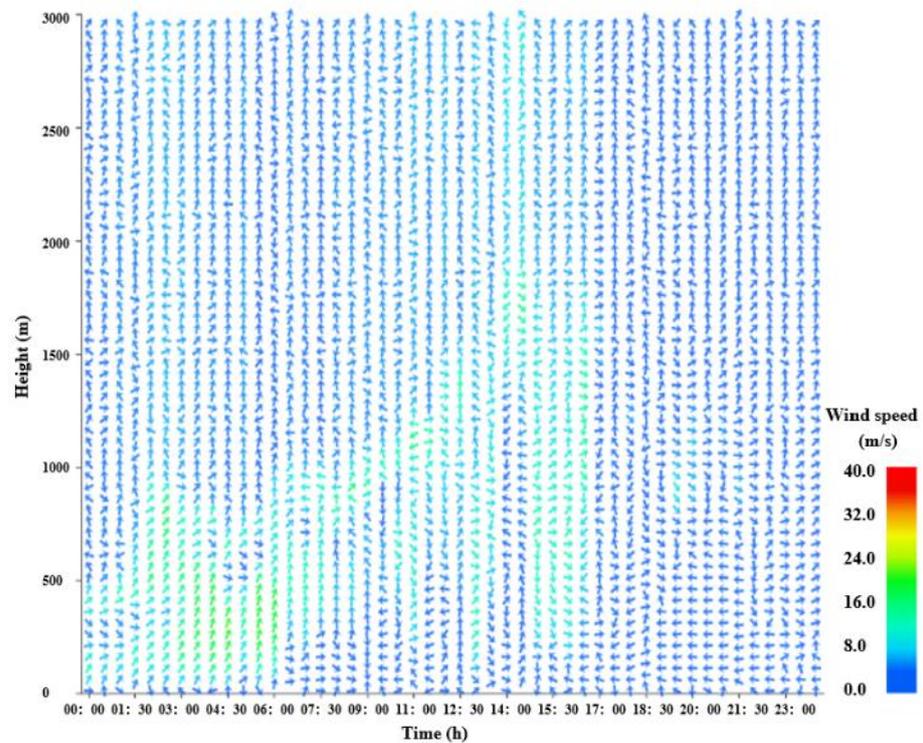

Figure 20. The results of wind speed and direction measured at the local ground-based weather station.

3.4.2. Pollution Characteristics of VOCs at Different Functional Areas

To further understand the pollution characteristics of VOCs at different functional areas of Hefei, VOC data were collected from three sampling sites using PTR-TOF-MS. The VOCs from the three different functional areas were broadly classified into three major categories: aromatic hydrocarbons (AHs), aliphatic hydrocarbons (ALHs), and oxygenated volatile organic compounds (OVOCs). Figure 21 shows the average concentration of different groups of VOCs observed throughout the navigation observation period. OVOCs accounted for a large proportion of total VOCs at all three sampling sites, followed by ALHs and AHs. The RA site had a relatively low concentration of total VOCs with a mean value of 92.8 ppb. The CD site was second with a mean value of 125.3 ppb. The IP site had a relatively high concentration of total VOCs with a mean value of 178.1 ppb, with OVOCs accounting for 65% of all VOCs, while AHs and ALHs accounted for 21% and 14%, respectively. The high proportion of OVOCs was mainly from industrial emissions at the IP site. At the RA and CD sites, OVOCs are likely emitted from vegetation and major human activities [44,45]. Individual analyses of the data from the three sampling sites were carried out to determine the chemical compositions of the VOCs further.
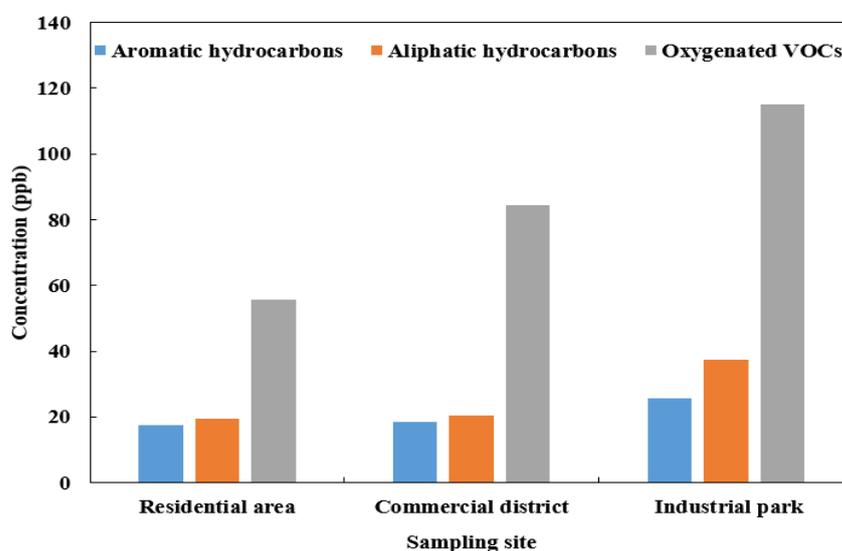

Figure 21. Concentrations of the different groups of VOCs were collected at the three sampling sites.

Figure 22 shows the percentages of individual VOCs. The compounds shown in red font in the legend are O_3 precursors.

Case 1: On 4 August 2021, at approximately 5:30 p.m., navigation monitoring was carried out about 80 m south of the kindergarten on Wangxi Road in Shushan District, Hefei (see Figure 22a). The concentrations of this region's top three O_3 precursors were 19.82 ppb, 15.84 ppb, and 15.33 ppb, respectively. The area reflects the characteristics of vehicle emissions and chemical solvents, with relatively high levels of aromatic hydrocarbons in VOCs [46]. In particular, the region exceeded the evening peak hour limit for methyl mercaptan, ethyl mercaptan, and butyl mercaptan; methyl mercaptan is an ozone precursor with a detected concentration of 0.49 ppb.

Case 2: On 5 August 2021, at around 11:00 a.m., navigation monitoring of the Hefei Economic Development Zone was carried out (see Figure 22b). Toluene is a component of the VOCs in the area, accounting for 51.47% of the total and detected at concentrations up to 48.7 ppb. There are many sources of toluene, which may be emitted from industrial activities, vehicle exhaust, and chemical solvents. The proportion of xylene/ethylbenzene, butene, and aniline also cannot be ignored.

Case 3: On 5 August 2021, at around 2:00 p.m., navigation monitoring was conducted downstream of the IP of Shushan District, Hefei. Among the VOCs (Figure 22c), xylene/ethylbenzene was the most abundant substance at the IP site, accounting for 78.97%

of the total top ten. This can be attributed to the presence of rubber and paint factories, where xylene/ethylbenzene is used as an essential chemical material in the production of rubber and paint. Meanwhile, VOCs such as aldehydes and ketones, which are products of the oxidation of hydrocarbons, can be detected in high quantities downstream of the contaminated area. The three case studies above show that the concentrations and compositions of VOCs have regional characteristics.
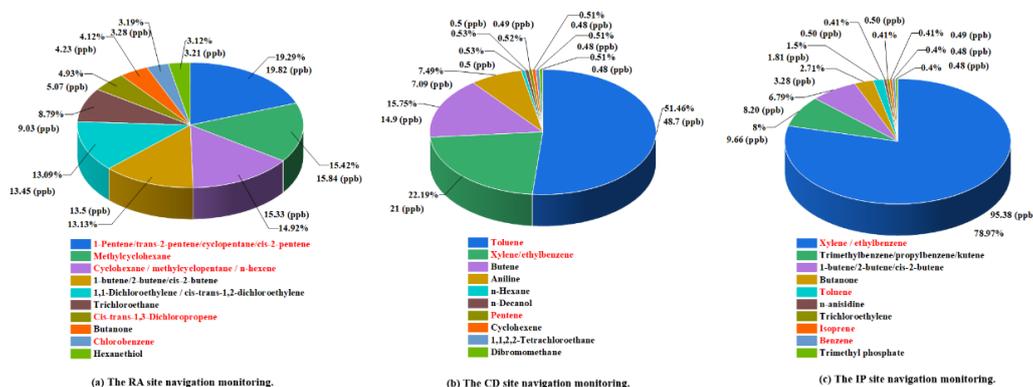

Figure 22. Percentages of individual VOCs.

3.4.3. The Connection between Wind Fields and VOCs

Atmospheric wind fields affect the transport and dispersion processes of pollutants through horizontal motion and vertical transport. A wind-dominated pollutant transport process was observed in the navigation monitoring of the IP site, and the variations in VOCs at different moments during this period are reflected in Figure 23. The six sub-plots given in Figure 23 were all collected in the vicinity of industrial plants in the industrial areas. VOCs are significant precursors of O_3 and secondary organic aerosols contributing to $PM_{2.5}$. Once VOCs are emitted into the ambient air, their levels in the atmosphere are determined by meteorological conditions and atmospheric chemical transformation conditions. The average diurnal variations in temperature, humidity, and wind level, from 0:00 on 4 August to 0:00 on 6 August 2021, are shown in Figure 24. The meteorological conditions fluctuated considerably during the two days of observation. The relationship between temperature and humidity follows an approximately opposite trend. At 6 am, temperatures remained low, and humidity remained high. As the temperature increased, the relative humidity gradually decreased. At around 16:00 p.m., the temperature reached a maximum of 34 °C, while the relative humidity dropped to a minimum of 62%. Wind speed was generally low, with the wind level remaining below level 3. However, the wind direction fluctuated widely with several instances of wind shear. The weather conditions were dominated by high temperatures and low humidity, and light wind prevailed during the observation period.

The variation in VOCs and O_3 concentrations under different wind speed conditions is shown in Figure 25. Wind is essential for the transport and dispersion of atmospheric pollutants. Under low wind speeds, the changes in the concentration of VOCs and O_3 were positively correlated to wind speed to a certain extent. As wind speed increased, the concentrations of VOCs and O_3 also partially increased. This was mainly because increased airflow promotes the volatilization of VOCs and facilitates the dispersion of VOCs and O_3 into the air, increasing local pollutant concentration. Under high wind speeds, the concentrations of VOCs and O_3 were negatively correlated with wind speed to a certain extent. Although windy weather allows for a rapid dilution and removal of pollutants, higher wind speeds can also lead to the long-range transport of particulate matter and the accumulation of high concentrations in the downwind direction, thus diluting the local pollutant concentration and decreasing VOC and O_3 concentrations.
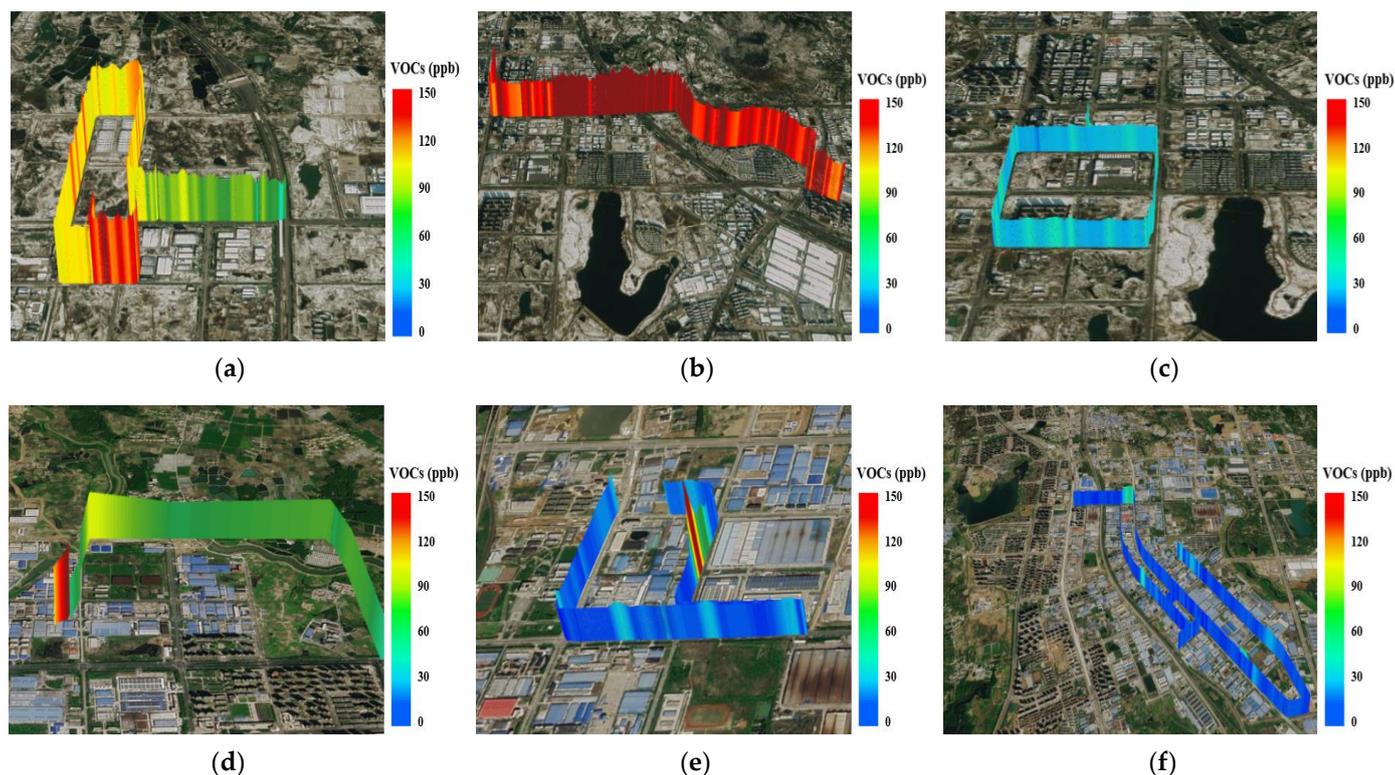
Figure 23. VOCs navigation monitoring: (**a**) 4 August 2021 16:30–17:00; (**b**) 4 August 2021 17:30–18:00; (**c**) 5 August 2021 00:30–01:00; (**d**) 4 August 2021 16:30–17:00; (**e**) 4 August 2021 17:30–18:00; (**f**) 5 August 2021 00:30–01:00.
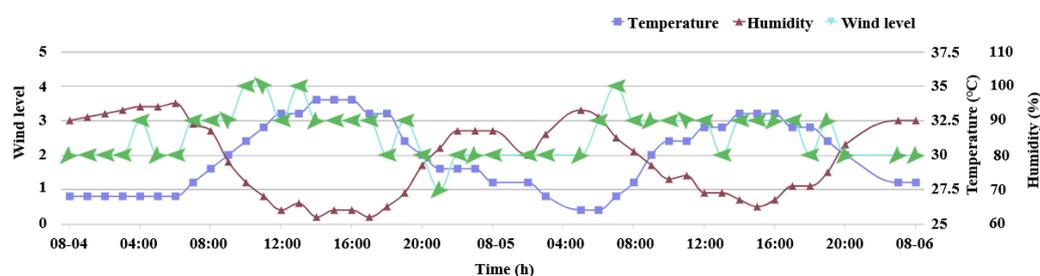

Figure 24. Variation trend of temperature, humidity, and wind level over time from 0:00 on 4 August to 0:00 on 6 August 2021.

In addition, a good correspondence between O_3 and VOCs can also be seen in Figure 25. O_3 concentration was single-peak, reaching its maximum value in the afternoon, while the VOC concentration underwent a bimodal change, reaching its maximum values in the morning and evening rush hours. The single peak of O_3 occurred at the trough of VOC concentrations. Before sunrise, light intensity was weak, with good overall air quality and no significant pollution. With stronger solar radiation, it is beneficial for VOCs to participate in photochemical reactions to produce ozone, and VOC concentration began to decline and O_3 concentrations gradually increased, reaching a peak at 15:00 (97 μg/m³). From afternoon to evening on the 4th, the VOC concentration increased from 26.3 ppb to 143.6 ppb due to one-day industrial emissions at the IP site. Meanwhile, with the decrease in solar radiation intensity and the weakening of atmospheric photochemical reactions, the continuous consumption of ozone precursors made the ozone concentration gradually decrease and stay low. The VOC concentration was negatively correlated with ozone concentration to some extent.
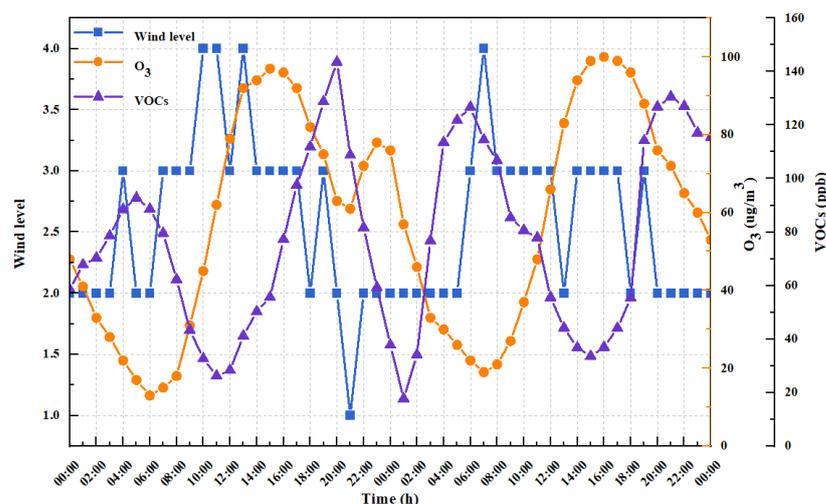
Figure 25. The average diurnal variation characteristics of wind level, O_3, and total VOC concentration during the navigation monitoring period.

In particular, from 20:00 to 22:00 on the 4th, the south wind turned to southeast wind, accompanied by a thunderstorm phenomenon and a small amount of high-altitude pollution transmission to the near ground, resulting in a higher ozone concentration near the ground. It is worth noting that there was light rain in the selected area on the night of the 4th, and the gradual accumulation of humidity caused the VOC concentration to decrease to 17.8 ppb in the early morning of the 5th. At around eight o'clock in the morning of the 5th, VOCs accumulated easily and quickly due to vehicle exhaust emissions, low wind speed, and high humidity.

As seen from the above observations, the VOCs at IP sites experience noticeable bimodal changes throughout the day. At the IP site, the VOC concentrations are at a low level during the night but gradually rise in the morning, peaking at around 8:00 a.m. At this time, motor vehicle emissions are the primary source of pollution in the area. Incomplete fuel combustion leads to higher pollutant levels when the vehicles slow down, accelerate, and are idle. As solar radiation increased gradually, photochemical reactions increased, atmospheric diffusion conditions improved, and the VOC concentration declined. It then drops and reaches the lowest level. After that, concentrations continue to increase, with another short-lived peak occurring at night. The reasons for this variation are closely related to the emission of pollution sources, meteorological conditions, and chemical reactions. At night, the atmospheric boundary layer is lower, and the wind vector is smaller, leading to a slower dispersion of pollutants. In addition, VOCs accumulate over long periods at night due to industrial emissions. Moreover, stronger solar radiation facilitates the participation of VOCs in photochemical reactions to produce ozone, and the oxidation of atmospheric VOCs with free radicals consumes large amounts of VOCs, thereby leading to a decrease in VOC concentrations.

4. Conclusions

In this work, the development of a vehicle-mounted CWML is reported based on the four-beam VAD scanning mode. The performance of the vehicle-mounted CWML is evaluated using calibration tests, comparison experiments, and continuous observation experiments. Additionally, the role of wind fields in the process of energy and material transport is studied comprehensively, which reveals that the local meteorological conditions, including wind speed and humidity, influence the VOC concentrations.

In short, the automatic correction of the wind speed and direction output can be realized by developing a new correction algorithm. The wind Lidar is applied to a vehicle to enhance mobility and realize multi-area real-time observation. The popularization of the vehicle-mounted CWML is expected to enable the realization of "flow observation station"

soon. Potentially, the vehicle-mounted CWML will be used for wind farm performance evaluation, aviation meteorological safety, and environmental monitoring.

References

1. Gupta, N.; Bhaskaran, P.K.; Dash, M.K. Recent trends in wind-wave climate for the Indian Ocean. *Curr. Sci.* **2015**, *108*, 2191–2201.
2. Xu, H.; Wang, W.-Y. A Method Based on Numerical Wind Field and Extreme Learning Machine for Typhoon Wind Speed Prediction of Wind Farm. *Math. Probl. Eng.* **2021**, *2021*, 7147973. [CrossRef]
3. Chan, P.; Shun, C.; Wu, K. Operational LIDAR-based system for automatic windshear alerting at the Hong Kong International Airport. In Proceedings of the 12th Conference on Aviation, Range, and Aerospace Meteorology, Atlanta, GA, USA, 27 January–3 February 2006.
4. Karthikeya, B.; Negi, P.S.; Srikanth, N. Wind resource assessment for urban renewable energy application in Singapore. *Renew. Energy* **2016**, *87*, 403–414. [CrossRef]
5. Morris, L. Second-generation LIDAR boosts wind power. *Power Eng.* **2011**, *115*, 50–54.
6. Rothermel, J.; Olivier, L.D.; Banta, R.M.; Hardesty, R.M.; Howell, J.N.; Cutten, D.R.; Johnson, S.C.; Menzies, R.T.; Tratt, D.M. Remote sensing of multi-level wind fields with high-energy airborne scanning coherent Doppler lidar. *Opt. Express* **1998**, *2*, 40–50. [CrossRef] [PubMed]
7. Kavaya, M.J.; Henderson, S.W.; Magee, J.R.; Hale, C.P.; Huffaker, R.M. Remote wind profiling with a solid-state Nd: YAG coherent lidar system. *Opt. Lett.* **1989**, *14*, 776–778. [CrossRef] [PubMed]
8. Diao, W.; Zhang, X.; Liu, J.; Zhu, X.; Liu, Y.; Bi, D.; Chen, W. All fiber pulsed coherent lidar development for wind profiles measurements in boundary layers. *Chin. Opt. Lett.* **2014**, *12*, 072801. [CrossRef]
9. Kameyama, S.; Ando, T.; Asaka, K.; Hirano, Y.; Wadaka, S. Compact all-fiber pulsed coherent Doppler lidar system for wind sensing. *Appl. Opt.* **2007**, *46*, 1953–1962. [CrossRef]
10. Huffaker, R.M. Laser Doppler detection systems for gas velocity measurement. *Appl. Opt.* **1970**, *9*, 1026–1039. [CrossRef] [PubMed]
11. Henderson, S.W.; Suni, P.J.; Hale, C.P.; Hannon, S.M.; Magee, J.R.; Bruns, D.L.; Yuen, E.H. Coherent laser radar at 2 mu m using solid-state lasers. *IEEE Trans. Geosci. Remote Sens.* **1993**, *31*, 4–15. [CrossRef]
12. Asaka, K.; Yanagisawa, T.; Hirano, Y. 1.5-um eye-safe coherent lidar system for wind velocity measurement. In *Lidar Remote Sensing for Industry and Environment Monitoring*; SPIE: Bellingham, WA, USA, 2001; pp. 321–328.
13. Chen, X.; Dai, G.; Wu, S.; Liu, J.; Yin, B.; Wang, Q.; Zhang, Z.; Qin, S.; Wang, X. Coherent high-spectral-resolution lidar for the measurement of the atmospheric Mie–Rayleigh–Brillouin backscatter spectrum. *Opt. Express* **2022**, *30*, 38060–38076. [CrossRef] [PubMed]
14. Shao, J.; Zhang, J.; Wang, W.; Zhang, S.; Yu, T.; Dong, W. Occurrence frequency of Kelvin-Helmholtz instability assessed by global high-resolution radiosonde and ERA5 reanalysis. *Atmos. Chem. Phys. Discuss.* **2023**, *2023*, 1–41. [CrossRef]
15. Lee, S.H.; Williams, P.D.; Frame, T.H.A. Increased shear in the North Atlantic upper-level jet stream over the past four decades. *Nature* **2019**, *572*, 639–642. [CrossRef]
16. Sathe, A.; Mann, J.; Vasiljevic, N.; Lea, G. A six-beam method to measure turbulence statistics using ground-based wind lidars. *Atmos. Meas. Tech.* **2015**, *8*, 729–740. [CrossRef]
17. Lane, S.; Barlow, J.F.; Wood, C.R. An assessment of a three-beam Doppler lidar wind profiling method for use in urban areas. *J. Wind Eng. Ind. Aerodyn.* **2013**, *119*, 53–59. [CrossRef]
18. Yang, Z.-H.; Zhang, Y.-K.; Zhou, J.; Chen, Y.; Zhang, G.-J.; Zhou, D.-F.; Chen, C.-L.; Hu, Y.-H.; Luo, X.; Feng, Z.-Z. Real-time wind field measurements using all-fiber mobile Doppler wind lidar. *Opt. Eng.* **2020**, *59*, 034107. [CrossRef]
19. Protat, A.; McRobert, I. Three-dimensional wind profiles using a stabilized shipborne cloud radar in wind profiler mode. *Atmos. Meas. Tech.* **2020**, *13*, 3609–3620. [CrossRef]
20. Zhai, X.; Wu, S.; Liu, B.; Song, X.; Yin, J. Shipborne Wind Measurement and Motion-induced Error Correction of a Coherent Doppler Lidar over the Yellow Sea in 2014. *Atmos. Meas. Tech.* **2018**, *11*, 1313–1331. [CrossRef]

21. Zhu, J.; Li, Z.; Liu, Z. Horizontal wind velocity retrieval using a Levenberg–Marquardt algorithm for an airborne wind lidar. *J. Appl. Remote Sens.* **2016**, *10*, 026009. [CrossRef]

22. Gasch, P.; Wieser, A.; Lundquist, J.K.; Kalthoff, N. An LES-based airborne Doppler lidar simulator and its application to wind profiling in inhomogeneous flow conditions. *Atmos. Meas. Tech.* **2020**, *13*, 1609–1631. [CrossRef]

23. Achtert, P.; Brooks, I.; Brooks, B.; Moat, B.; Prytherch, J.; Persson, P.; Tjernström, M. Measurement of wind profiles by motion-stabilised shipborne Doppler lidar. *Atmos. Meas. Tech.* **2015**, *8*, 4993–5007. [CrossRef]

24. Kelberlau, F.; Neshaug, V.; Lønseth, L.; Bracchi, T.; Mann, J. Taking the motion out of floating Lidar: Turbulence intensity estimates with a continuous-wave wind lidar. *Remote Sens.* **2020**, *12*, 898. [CrossRef]

25. Kotake, N.; Sakamaki, H.; Imaki, M.; Miwa, Y.; Ando, T.; Yabugaki, Y.; Enjo, M.; Kameyama, S. Intelligent and compact coherent Doppler lidar with fiber-based configuration for robust wind sensing in various atmospheric and environmental conditions. *Opt. Express* **2022**, *30*, 20038–20062. [CrossRef]

26. Richardson, S.D. Environmental mass spectrometry: Emerging contaminants and current issues. *Anal. Chem.* **2008**, *80*, 4373–4402. [CrossRef] [PubMed]

27. Biasioli, F.; Yeretzian, C.; Märk, T.D.; Dewulf, J.; Van Langenhove, H. Direct-injection mass spectrometry adds the time dimension to (B) VOC analysis. *TrAC Trends Anal. Chem.* **2011**, *30*, 1003–1017. [CrossRef]

28. Jin, S.; Li, J.; Han, H.; Wang, H.; Chu, Y.; Zhou, S. Proton transfer reaction mass spectrometry for online detection of trace volatile organic compounds. *Prog. Chem.* **2007**, *19*, 996.

29. Xue-Fang, Z.; Yi-Xiang, D. Proton Transfer Reaction-Mass Spectrometry for Online Analysis of Trace Volatile Organic Compounds. *Chin. J. Anal. Chem.* **2011**, *39*, 1611–1618.

30. Zhao, Y.F.; Zhang, X.J.; Zhang, Y.R.; Ding, J.X.; Wang, K.; Gao, Y.H.; Su, R.S.; Fang, J. Data Processing and Analysis of Eight-Beam Wind Profile Coherent Wind Measurement Lidar. *Remote Sens.* **2021**, *13*, 3549. [CrossRef]

31. Manninen, A.J.; Marke, T.; Tuononen, M.; O'Connor, E.J. Atmospheric Boundary Layer Classification With Doppler Lidar. *J. Geophys. Res.-Atmos.* **2018**, *123*, 8172–8189. [CrossRef]

32. Wang, X.; Cai, Y.; Wang, J.; Zhao, Y. Concentration monitoring of volatile organic compounds and ozone in Xi'an based on PTR-TOF-MS and differential absorption lidar. *Atmos. Environ.* **2021**, *245*, 118045. [CrossRef]

33. Pan, Y.; Zhang, Q.; Zhou, W.; Zou, X.; Wang, H.; Huang, C.; Shen, C.; Chu, Y. Detection of ketones by a novel technology: Dipolar proton transfer reaction mass spectrometry (DP-PTR-MS). *J. Am. Soc. Mass Spectrom.* **2017**, *28*, 873–879. [CrossRef] [PubMed]

34. Zhao, J.; Zhang, R. Proton transfer reaction rate constants between hydronium ion (H3O+) and volatile organic compounds. *Atmos. Environ.* **2004**, *38*, 2177–2185. [CrossRef]

35. Salcedo-Bosch, A.; Rocadenbosch, F.; Sospedra, J. A robust adaptive unscented kalman filter for floating doppler wind-lidar motion correction. *Remote Sens.* **2021**, *13*, 4167. [CrossRef]

36. Savage, P.G. Strapdown inertial navigation integration algorithm design part 1: Attitude algorithms. *J. Guid. Control Dyn.* **1998**, *21*, 19–28. [CrossRef]

37. Savage, P.G. Strapdown inertial navigation integration algorithm design part 2: Velocity and position algorithms. *J. Guid. Control Dyn.* **1998**, *21*, 208–221. [CrossRef]

38. Salonen, K.; Järvinen, H.; Eresmaa, R.; Niemelä, S. Bias estimation of Doppler-radar radial-wind observations. *Q. J. R. Meteorol. Soc. A J. Atmos. Sci. Appl. Meteorol. Phys. Oceanogr.* **2007**, *133*, 1501–1507. [CrossRef]

39. Lin, R.Q.; Guo, P.; Chen, H.; Chen, S.Y.; Zhang, Y.C. Smoothed accumulated spectra based wDSWF method for real-time wind vector estimation of pulsed coherent Doppler lidar. *Opt. Express* **2022**, *30*, 180–194. [CrossRef]

40. Scholkmann, F.; Boss, J.; Wolf, M. An Efficient Algorithm for Automatic Peak Detection in Noisy Periodic and Quasi-Periodic Signals. *Algorithms* **2012**, *5*, 588–603. [CrossRef]

41. Zhang, H.; Wu, S.; Wang, Q.; Liu, B.; Yin, B.; Zhai, X. Airport low-level wind shear lidar observation at Beijing Capital International Airport. *Infrared Phys. Technol.* **2019**, *96*, 113–122. [CrossRef]

42. Abdelazim, S.; Santoro, D.; Arend, M.; Moshary, F.; Ahmed, S. A hardware implemented autocorrelation technique for estimating power SPectral density for processing signals from a Doppler wind Lidar system. *Sensors* **2018**, *18*, 4170. [CrossRef]

43. Frehlich, R.; Kelley, N. Measurements of Wind and Turbulence Profiles With Scanning Doppler Lidar for Wind Energy Applications. *Ieee J. Sel. Top. Appl. Earth Obs. Remote Sens.* **2008**, *1*, 42–47. [CrossRef]

44. Yu, Y.; Wen, S.; Lü, H.; Feng, Y.; Wang, X.; Sheng, G.; Fu, J. Characteristics of atmospheric carbonyls and VOCs in Forest Park in South China. *Environ. Monit. Assess.* **2008**, *137*, 275–285. [CrossRef] [PubMed]

45. Ling, Z.; Guo, H.; Chen, G.; Lam, S.H.M.; Fan, S. Formaldehyde and acetaldehyde at different elevations in mountainous areas in Hong Kong. *Aerosol Air Qual. Res.* **2016**, *16*, 1868–1878. [CrossRef]

46. Dumanoglu, Y.; Kara, M.; Altiok, H.; Odabasi, M.; Elbir, T.; Bayram, A. Spatial and seasonal variation and source apportionment of volatile organic compounds (VOCs) in a heavily industrialized region. *Atmos. Environ.* **2014**, *98*, 168–178. [CrossRef]